Journal of Power Sources 185 (2008) 876–880

Contents lists available at ScienceDirect

Journal of Power Sources

journal homepage: www.elsevier.com/locate/jpowsour

Short communication

Effect of Sm substitution for Gd on the electrical conductivity of fluorite-type $Gd_2Zr_2O_7$

Zhan-Guo Liu, Jia-Hu Ouyang*, Yu Zhou, Xiao-Liang Xia

Institute for Advanced Ceramics, Department of Materials Science, Harbin Institute of Technology, Harbin 150001, China

ARTICLE INFO

Article history:
Received 21 July 2008
Received in revised form 2 September 2008
Accepted 3 September 2008
Available online 9 September 2008

Keywords:
$Gd_{2-x}Sm_xZr_2O_7$
Electrical conductivity
Impedance spectroscopy
Substitution

ABSTRACT

$Gd_{2-x}Sm_xZr_2O_7$ ($x = 0$, 0.2, 0.6, 1.0, 1.4, 1.8, 2.0) ceramic powders synthesized with the chemical-coprecipitation and calcination method were pressureless-sintered at 1873 K for 10 h in air. The electrical conductivity of $Gd_{2-x}Sm_xZr_2O_7$ ceramics was investigated by complex impedance spectroscopy over a frequency range of 0.01 Hz to 15 MHz. $Gd_{2-x}Sm_xZr_2O_7$ is an oxide-ion conductor in the oxygen partial pressure range from 1.0×10^{-15} to 1.0 atm and in the temperature range of 623–873 K. The measured electrical conductivity obeys the Arrhenius relation. The activation energy and pre-exponential factor for grain-interior conductivity gradually decrease with increasing Sm content. The grain-interior conductivity varies with the Sm substitution for Gd, and reaches the maximum at the equal molar of Sm^{3+} and Gd^{3+} in $Gd_{2-x}Sm_xZr_2O_7$ ceramics. A significant increase in the grain-interior conductivity is obtained by isovalent rare-earth element like Sm substitution for Gd in the temperature range of 623–873 K.

1. Introduction

Complex oxides with the general formula $Ln_2Zr_2O_7$ (Ln = lanthanide) exhibit an ordered pyrochlore-type structure or a defective fluorite-type structure, which is mainly governed by the ionic radius ratio of Ln^{3+} and Zr^{4+} [1]. These compounds have a wide variety of interesting physical and chemical properties, which make them suitable for applications as catalysts, solid electrolytes, nuclear waste forms, thermal barrier coatings, etc. [2–5]. Their electrical properties make them potential candidates for solid oxide fuel cells applications. The oxide ion conductivity of $Gd_2(Zr_{0.3}Ti_{0.69}Ta_{0.01})_2O_7$ exhibited a mixed conductivity in an oxygen partial pressure range of 1.0×10^{-18} to 1.0 atm and in a temperature range of 1073–1373 K [6]. The advantage of lowering the operation temperature of solid oxide fuel cells has attracted great interest worldwide. Enormous amounts of efforts can be found in the literature on ionic conductivity improvements for the oxide electrolyte materials [7,8]. van Dijk et al. [9,10] prepared $Gd_xZr_{1-x}O_{2-x/2}$ ($0.2 < x < 0.6$) ceramics by a wet chemical method, and found that the stoichiometric $Gd_2Zr_2O_7$ pyrochlore phase had a maximum in ionic conductivity and a minimum in activation energy at temperatures between 773 and 1023 K. EMF measurements demonstrated that the conductivity of cubic ZrO_2–Gd_2O_3 solid solutions was almost purely ionic at temperatures of 773–1023 K and oxygen partial pressures of 0.2 and 1.0 atm [9]. The conductivity of $Sm_2Zr_2O_7$ pyrochlore phase was comparable to those of other good oxide-ion conductors in low-temperature regions [11]. At 1087 K, the conductivity of $Sm_2Zr_2O_7$ was approximately constant in an oxygen partial pressure range of $1–10^{-20}$ atm, which is typical of the oxide-ion conductor. However, with the increase of temperature up to 1381 K, the conductivity of $Sm_2Zr_2O_7$ tended to increase slightly at the low and high oxygen partial pressures. The increased conductivity at the low and high oxygen partial pressures suggests that the electrons and electron holes started to contribute to the total conductivity at elevated temperatures [11]. New rare-earth zirconates doped with cations of different ionic radius ratio are of considerable scientific interest. $Gd_2Zr_2O_7$ doped with 5 and 10 mol% Sr at the Gd sites showed a higher total conductivity than pure $Gd_2Zr_2O_7$ in the temperature range of 773–973 K [12]. Mandal et al. [13] synthesized $Gd_{2-x}Nd_xZr_2O_7$ ($0 \le x \le 2.0$) by a solid-state reaction route, and found that a significant increase in electrical conductivity can be obtained at 622–696 K. Díaz-Guillén et al. [14] prepared $Gd_{2-y}La_yZr_2O_7$ ($0 \le y \le 2.0$) solid solutions by mechanochemical synthesis, and found that $Gd_{2-y}La_yZr_2O_7$ showed a higher oxide-ion conductivity value for $0 \le y \le 1.0$ than those for $1.0 < y \le 2.0$ in the temperature range of 473–1273 K.

In this work, $Gd_{2-x}Sm_xZr_2O_7$ ($0 \le x \le 2.0$) ceramic powders were synthesized by the chemical-coprecipitation and calcination method, and were then pressureless-sintered at 1873 K for 10 h in air. The effect of the Sm substitution for Gd on the electrical conductivity of fluorite-type $Gd_2Zr_2O_7$ was investigated.

* Corresponding author. Tel.: +86 451 86414291; fax: +86 451 86414291.
E-mail address: ouyangjh@hit.edu.cn (J.-H. Ouyang).

0378-7753/$ – see front matter © 2008 Elsevier B.V. All rights reserved.
doi:10.1016/j.jpowsour.2008.09.005

2. Experimental procedure

In the present study, $ZrOCl_2{\cdot}8H_2O$ (Zibo Huantuo Chemical Co., Ltd., Zibo, China; Analytical), Gd_2O_3 and Sm_2O_3 (Rare-Chem Hi-Tech Co., Ltd., Huizhou, China; purity ≥99.99%) were chosen as the reactants. Ceramic powders of $Gd_{2-x}Sm_xZr_2O_7$ (x = 0, 0.2, 0.6, 1.0, 1.4, 1.8, 2.0) were synthesized by the chemical-coprecipitation and calcination method. Gd_2O_3 and Sm_2O_3 powders were calcined at 1173 K for 2 h to remove any absorbed moisture before weighing. For each composition, Gd_2O_3 and Sm_2O_3 were weighed, and dissolved in dilute nitric acid, while $ZrOCl_2{\cdot}8H_2O$ was dissolved in distilled water. These solutions were mixed, stirred, filtered and slowly added to dilute ammonium hydrate solution to obtain gel-like precipitates. These gels were washed with distilled water several times to a pH value of 7, and then washed with absolute alcohol twice. The washed precipitates were dried at 373 K over night. The remaining solid was calcined at 1073 K for 5 h in air and compacted by cold isostatic pressing at 280 MPa for 5 min. Finally, the compacts were pressureless-sintered at 1873 K for 10 h in air.

Crystal structures of synthesized powders and sintered ceramics were identified by an X-ray diffractometer (D/Max-2200VPC, Rigaku Co., Ltd., Japan) with Cu Kα radiation at a scan rate of 4°/min. The morphologies of synthesized powders and sintered ceramics were observed by scanning electron microscope (SEM, Hitachi S-4800, Japan). SEM specimens of bulk ceramics were polished with 1 μm diamond paste, and then thermally etched at 1773 K for 1 h in air. A thin carbon coating was evaporated onto the surface of the specimens for electrical conductivity. Qualitative X-ray elemental analysis of specimens was carried out using SEM equipped with energy dispersive spectroscopy (EDS). The bulk density of the samples was measured by the Archimedes principle with an immersion medium of deionized water. The theoretical density of the specimens was calculated using lattice parameters acquired from XRD results and the chemical formula weight in a unit cell.

Cylindrical disc-shaped specimens with a diameter of 12.5 mm and a thickness of approximate 1.5 mm were machined from the sintered samples and ground so that both surfaces were coplanar. Both the front and the rear surfaces of each pellet were coated with a silver paste (DAD-87 type). Each pellet was then heated to 973 K for 1 h with a heating rate of 5 K min^{-1} in order to ensure intimate contact with the specimen surface and eliminate organic components. The complex impedance spectra of the pellets were measured using the four-probe method with a computerized Solatron™ SI 1260 impedance/gain-phase analyzer combined with a Solatron™ SI 1287 electrochemical interface over a frequency range of 0.01 Hz to 15 MHz in air. The measurements were carried out during cooling from 873 to 623 K at a 50 K interval with a cooling rate of 5 K min^{-1} and a stabilisation time of 20 min between consecutive measurements. A K-type thermocouple was positioned adjacent to the specimen in order to monitor the specimen temperature. Oxygen partial pressure $p(O_2)$ dependence of the electrical conductivity was also measured in the $p(O_2)$ range of 1.0×10^{-15} to 1.0 atm. Measurements were performed in a closed tube furnace from 873 to 623 K during cooling. The $p(O_2)$ values were monitored with an YSZ oxygen sensor placed close to the specimen.

3. Results and discussion

Fig. 1 reveals the X-ray diffraction patterns of $Sm_2Zr_2O_7$ powder calcined at different temperatures and holding times. It can be seen that $Sm_2Zr_2O_7$ powder completely crystallizes at 1073 K for 5 h in air. $Sm_2Zr_2O_7$ powder calcined at 1073 K for 5 h has wide diffraction peaks, and exhibits a single phase of cubic structure, owing to fine grains. Fig. 2 shows typical morphology of $GdSmZr_2O_7$ powder calcined at 1073 K for 5 h firing. From SEM observations, $GdSmZr_2O_7$ powder has a particle size of about 100 nm in diameter, and exhibits to a certain extent agglomeration.

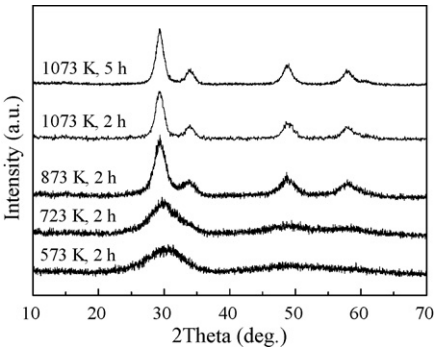

Fig. 1. XRD patterns of $Sm_2Zr_2O_7$ powder calcined at different temperatures and holding times.

The XRD patterns of $Gd_{2-x}Sm_xZr_2O_7$ ceramics sintered at 1873 K for 10 h were recorded and analyzed. The diffraction patterns of $Gd_{2-x}Sm_xZr_2O_7$ (x = 0, 0.2, 1.0, 2.0) specimens are shown in Fig. 3. All $Gd_{2-x}Sm_xZr_2O_7$ ceramics have a single phase. $Gd_2Zr_2O_7$ exhibits a defective fluorite-type structure. However, $Gd_{2-x}Sm_xZr_2O_7$ ($0.2 \le x \le 2.0$) ceramics have an ordered pyrochlore-type structure, which is characterized by the presence of typical superstructure diffraction peaks at the 2θ values of about 14° (1 1 1), 28° (3 1 1), 37° (3 3 1), 45° (5 1 1) and 51° (5 3 1) using Cu Kα radiation [15,16], as shown in Fig. 3. $Gd_2Zr_2O_7$ and $Sm_2Zr_2O_7$ ceramics form continuous solid solution.

In the $Ln_2Zr_2O_7$ system, the phase structure is mainly determined by the ionic radius ratio of $r(Ln^{3+})/r(Zr^{4+})$. The stability of pyrochlore structure in zirconates at one atmospheric pressure is limited to the range of $1.46 \le r(Ln^{3+})/r(Zr^{4+}) \le 1.78$ [1]. The ionic radius of Zr^{4+} is 0.72 Å in the six-coordinated; however, the ionic radius of Sm^{3+} and Gd^{3+} are 1.079 Å and 1.053 Å in the eightfold coordination [17], respectively. For $Gd_2Zr_2O_7$, the $r(Gd^{3+})/r(Zr^{4+})$ is equal to 1.46, which resides at the edge of the pyrochlore phase stability window. It is well known that $Gd_2Zr_2O_7$ undergoes a pyrochlore to fluorite (order–disorder) transition when heated to above 1803 K [18]. As the sintering temperature used in this work (1873 K) is higher than the order–disorder transition temperature, it is not surprising that $Gd_2Zr_2O_7$ exhibits a defective fluorite-type structure. As for other zirconate ceramics of $Gd_{2-x}Sm_xZr_2O_7$

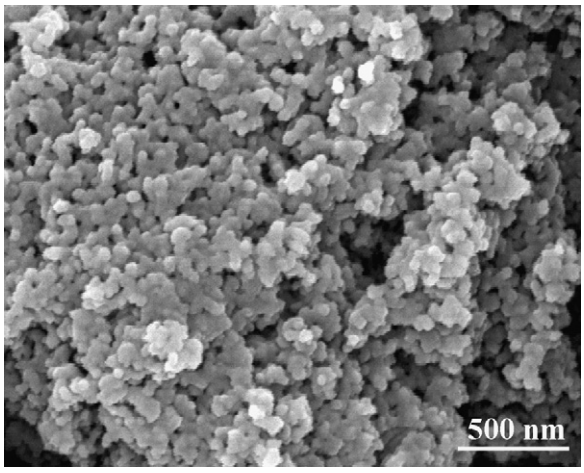

Fig. 2. Typical morphology of $GdSmZr_2O_7$ ceramic powder calcined at 1073 K for 5 h.

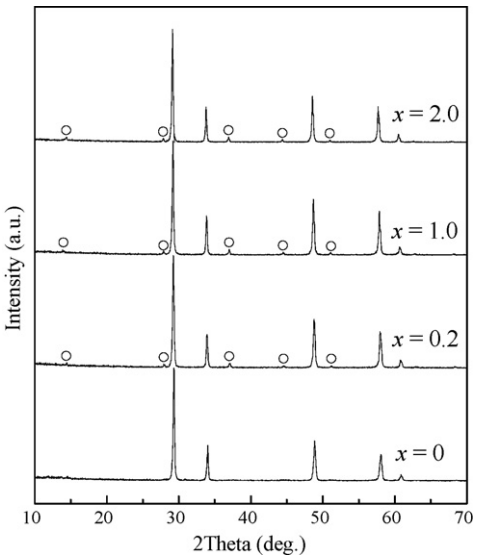

Fig. 3. XRD patterns of $Gd_{2-x}Sm_xZr_2O_7$ ($x = 0, 0.2, 1.0, 2.0$) ceramics. The symbol "○" represents the superstructure diffraction peaks.

Table 1
Relative densities and chemical compositions of $Gd_{2-x}Sm_xZr_2O_7$ ceramics

Ceramic materials	Relative density (%)	Mol ratio		
		Sm	Gd	Zr
$Gd_2Zr_2O_7$	92.3	0	49.7	50.3
$Sm_{0.2}Gd_{1.8}Zr_2O_7$	93.1	5.1	44.7	50.2
$Sm_{0.6}Gd_{1.4}Zr_2O_7$	93.2	14.8	35.1	50.1
$Sm_{1.0}Gd_{1.0}Zr_2O_7$	96.7	24.9	24.9	50.2
$Sm_{1.4}Gd_{0.6}Zr_2O_7$	94.8	34.8	14.8	50.4
$Sm_{1.8}Gd_{0.2}Zr_2O_7$	93.2	44.9	4.9	50.2
$Sm_2Zr_2O_7$	97.5	49.9	0	50.1

($0.6 \le x \le 2.0$), the value of $r(Ln^{3+})/r(Zr^{4+})$ is obviously higher than 1.46, $Gd_{2-x}Sm_xZr_2O_7$ ($0.6 \le x \le 2.0$) ceramics exhibit an ordered pyrochlore-type structure. Therefore, the degree of structure ordering of $Sm_2Zr_2O_7$ is much higher than that of $Gd_2Zr_2O_7$.

The relative (bulk to X-ray) densities of $Gd_{2-x}Sm_xZr_2O_7$ ceramics are in the range of 92.3–97.5%, as shown in Table 1. Fig. 4 shows the typical microstructure of $GdSmZr_2O_7$. The average grain size of $GdSmZr_2O_7$ is several micrometers, and the grain boundaries

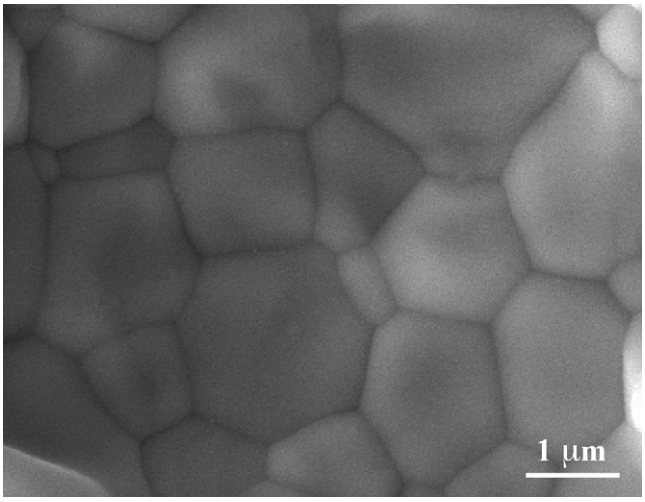

Fig. 4. Microstructure of $GdSmZr_2O_7$.

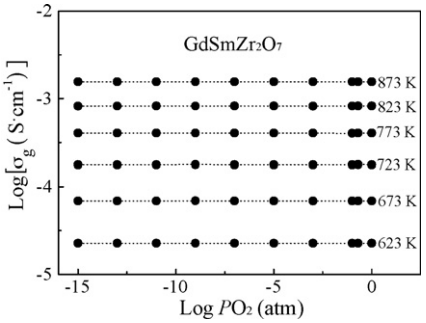

Fig. 5. Oxygen partial pressure dependence of the electrical conductivity of $GdSmZr_2O_7$ at different temperatures.

in $GdSmZr_2O_7$ are very clean. The chemical compositions of sintered ceramics were determined by EDS. Table 1 shows the results of chemical compositions for $Gd_{2-x}Sm_xZr_2O_7$ ceramics. According to EDS analyses, the mol ratio of different metallic elements in $Gd_{2-x}Sm_xZr_2O_7$ ceramics is ±2% different from stoichiometry.

The oxygen partial pressure $p(O_2)$ dependence of electrical conductivity was measured for $Gd_{2-x}Sm_xZr_2O_7$ ceramics. Fig. 5 shows the electrical conductivity of $GdSmZr_2O_7$ as a function of oxygen partial pressure $p(O_2)$ at different temperatures. It is clearly seen that electrical conductivity of $GdSmZr_2O_7$ is almost independent of oxygen partial pressure from 1.0×10^{-15} to 1.0 atm at different temperature levels from 873 to 623 K, which indicates a pure oxide-ion conductivity with negligible electronic conduction [19]. Fig. 6 shows typical complex impedance plots of $GdSmZr_2O_7$ measured at 623 and 673 K in air. Three distinct contributions manifested in the form of semicircular arcs are

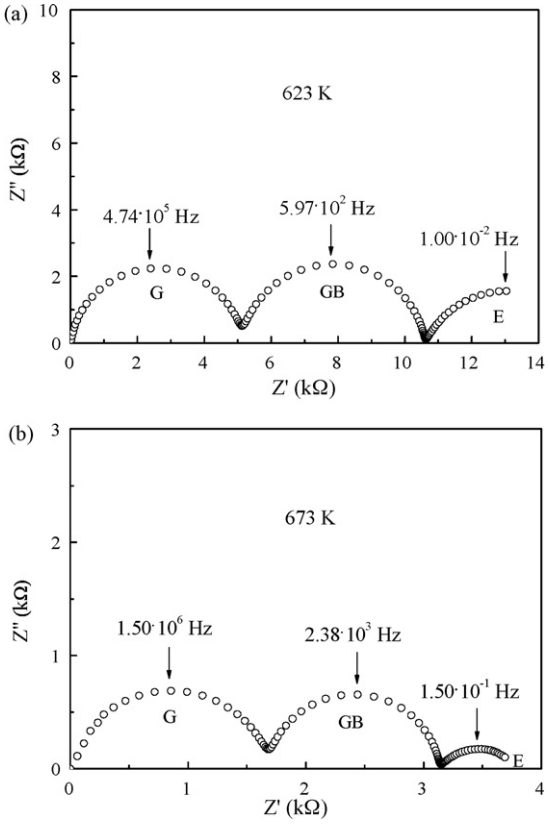

Fig. 6. Typical complex impedance plots for $GdSmZr_2O_7$ at (a) 623 and (b) 673 K. The grain-interior (G), grain-boundary (GB) and electrode (E) contributions are also indicated.

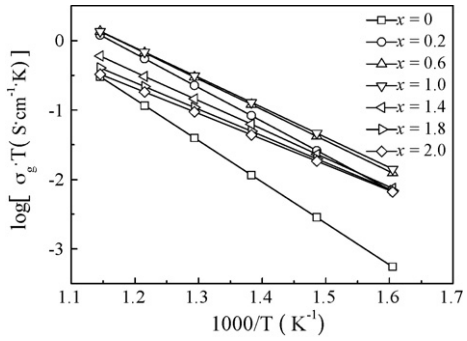

Fig. 7. Arrhenius plots of the grain-interior (G) conductivity of $Gd_{2-x}Sm_xZr_2O_7$ ceramics.

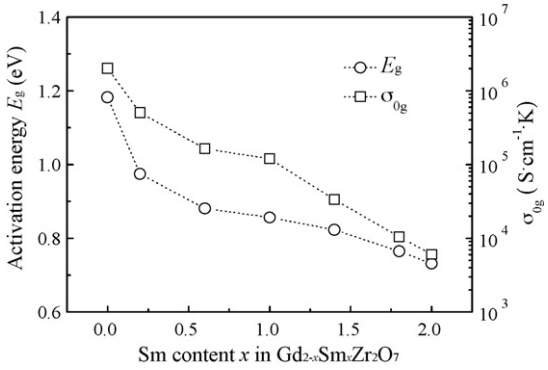

Fig. 8. Activation energy E_g and pre-exponential factor σ_{0g} of $Gd_{2-x}Sm_xZr_2O_7$ ceramics for the grain-interior conductivity as a function of the Sm content.

identified in Fig. 6. The high frequency semicircle corresponds to the grain-interior impedance, the intermediate-range frequency semicircle represents the grain-boundary impedance, and the low frequency semicircle is due to the polarization effects from charge carrier blocking at the electrodes. From Fig. 6(a), capacitance values found for the high-, intermediate- and low-frequency arcs are 2.36×10^{-10}, 9.32×10^{-8} and 1.31×10^{-3} F/cm at 623 K, which corresponds to the grain-interior, grain boundary and electrodes polarization contributions, respectively. However, at 673 K, capacitance values found for the high-, intermediate- and low-frequency arcs are 8.32×10^{-11}, 1.24×10^{-7} and 1.78×10^{-3} F/cm, as shown in Fig. 6(b). Typical equivalent electrical circuit applied to reproduce such impedance plots consists of parallel resistance–capacitance (R–C) blocks connected in series [20]. These three contributions are separated by fitting semicircles to each of the arcs, and the grain-interior resistance values, R_g are determined from the intercepts of high frequency-range frequency semicircles on the Z′ axes [21], respectively. The electrical conductivity at different temperatures is calculated from the resistance values and the dimensions of the specimens.

The temperature dependence of the grain-interior conductivity is analyzed using an Arrhenius equation with the following expression:

$$\sigma_g T = \sigma_0 \exp\left(-\frac{E}{k_B T}\right) \quad (1)$$

where pre-exponential factor σ_0 is a measurement of the effective number of mobile oxide-ions, E is the activation energy for the electrical conduction process, k_B is the Boltzmann constant, and T is absolute temperature. Fig. 7 shows the Arrhenius plots of the grain-interior conductivity of $Gd_{2-x}Sm_xZr_2O_7$ ceramics. The values of activation energy (E_g) and pre-exponential factor (σ_{0g}) for each composition are calculated from the slope and the intercept of the linear fits in the Arrhenius plots (Fig. 6), respectively. The calculated values of activation energy and pre-exponential factor are presented in Table 2.

The activation energy E_g and pre-exponential factor σ_{0g} of $Gd_{2-x}Sm_xZr_2O_7$ ceramics for the grain-interior conductivity as a function of the Sm content are shown in Fig. 8. The activation energy E_g gradually decreases with increasing Sm content. Similar phenomena were found in the case of $Gd_{2-x}Nd_xZr_2O_7$ system. The activation energy gradually decreased with increasing Nd content in $Gd_{2-x}Nd_xZr_2O_7$ [13]. The activation energy E_g of $Gd_2Zr_2O_7$ in this study is 1.18 eV, which is consistent with van Dijk et al.'s results [9]. The activation energy E_g of $Sm_2Zr_2O_7$ in this study is 0.73 eV, which is slightly higher than Shinozaki et al.'s results [11]. From Fig. 8, the pre-exponential factor σ_{0g} has a similar tendency to activation energy E_g. It gradually decreases with increasing Sm content, indicating that the effective number of mobile oxide ions decreases due to the Sm substitution for Gd in $Gd_{2-x}Sm_xZr_2O_7$ ceramics. This is in good agreement with the XRD results, which indicates that the degree of ordering becomes greater when the Sm content x increases from $x = 0$ ($Gd_2Zr_2O_7$) to $x = 2.0$ ($Sm_2Zr_2O_7$).

Fig. 9 presents the variations of the grain-interior conductivity of $Gd_{2-x}Sm_xZr_2O_7$ ceramics as a function of the Sm content. Clearly, the grain-interior conductivity increases with increasing temperature for each composition. With the increase of the Sm content x, the grain-interior conductivity σ_g rapidly increases from pure $Gd_2Zr_2O_7$ ($x = 0$) to $Gd_{1.8}Sm_{0.2}Zr_2O_7$ ($x = 0.2$), and reaches the maximum at the equal molar ($x = 1.0$) of Sm^{3+} and Gd^{3+} in the $Gd_{2-x}Sm_xZr_2O_7$ system, and then decreases with further increasing Sm content. A significant increase in electrical conductivity is obtained by isovalent rare-earth element like Sm substitution for Gd in the temperature range of 623–873 K. The highest electrical conductivity value obtained in this study reaches 1.56×10^{-3} S cm^{-1} at 873 K for $GdSmZr_2O_7$. The increase in σ_g would lead to an increase in electrical conductivity; however, the

Table 2
Activation energy E and pre-exponential factor σ_0 for the grain-interior (G) contributions to conductivity

Ceramic materials	Grain-interior (G) contributions	
	Activation energy, E_g (eV)	Pre-exponential factor, σ_{0g} (S cm^{-1} K)
$Gd_2Zr_2O_7$	1.18	2.01×10^6
$Sm_{0.2}Gd_{1.8}Zr_2O_7$	0.97	5.06×10^5
$Sm_{0.6}Gd_{1.4}Zr_2O_7$	0.88	1.64×10^5
$Sm_{1.0}Gd_{1.0}Zr_2O_7$	0.86	1.20×10^5
$Sm_{1.4}Gd_{0.6}Zr_2O_7$	0.82	3.36×10^4
$Sm_{1.8}Gd_{0.2}Zr_2O_7$	0.76	1.05×10^4
$Sm_2Zr_2O_7$	0.73	6.02×10^3

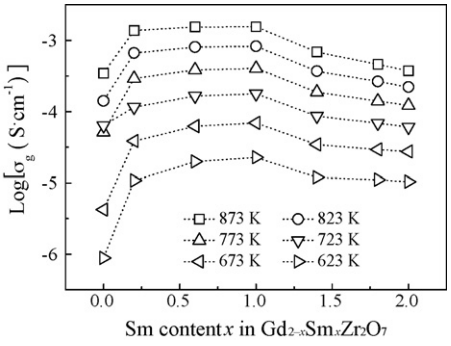

Fig. 9. Variations of the grain-interior (G) conductivity of $Gd_{2-x}Sm_xZr_2O_7$ ceramics as a function of the Sm content.

increase in E_g would hinder the oxide ion migration. Thus, these two processes are competing. As the Sm content further increases from 1.0 to 2.0, both σ_g and E_g decrease as shown in Fig. 8. From Fig. 9, the electrical conductivity of $Gd_{2-x}Sm_xZr_2O_7$ ($1.0 \le x \le 2.0$) decreases with increasing Sm content. This indicates that the decrease in E_g is not able to compensate for the decrease in the effective number of mobile oxide ions, and finally causes the drop in electrical conductivity.

4. Conclusions

(1) $Gd_2Zr_2O_7$ exhibits a defective fluorite-type structure. However, $Gd_{2-x}Sm_xZr_2O_7$ ($0.2 \le x \le 2.0$) ceramics have an ordered pyrochlore-type structure. The degree of structure ordering for $Gd_{2-x}Sm_xZr_2O_7$ ceramics increases with increasing Sm content.

(2) $Gd_{2-x}Sm_xZr_2O_7$ ceramics are oxide-ion conductor in an oxygen partial pressure from 1.0×10^{-15} to 1.0 atm and in the temperature range of 623–873 K. The grain-interior conductivity of $Gd_{2-x}Sm_xZr_2O_7$ ($x = 0$, 0.2, 0.6, 1.0, 1.4, 1.8, 2.0) ceramics varies with the Sm substitution for Gd in the temperature range of 623–873 K. A significant increase in electrical conductivity is obtained by isovalent rare-earth element like Sm substitution for Gd in the temperature range of 623–873 K. The grain-interior conductivity reaches the highest value of 1.56×10^{-3} S cm^{-1} at 873 K for $GdSmZr_2O_7$.

Acknowledgements

The authors would like to thank the financial support from the Program of Excellent Teams in Harbin Institute of Technology (HIT) and the Start-up Program for High-level HIT Faculty Returned from Abroad.

References

[1] M.A. Subramanian, G. Aravamudan, G.V. Subba Rao, Prog. Solid State Chem. 15 (1983) 55–143.
[2] J.M. Sohn, M.R. Kim, S.I. Woo, Catal. Today 83 (2003) 289–297.
[3] A.V. Shlyakhtina, A.V. Knotko, M.V. Boguslavskii, S.Yu. Stefanovich, I.V. Kolbanev, L.L. Larina, L.G. Shcherbakova, Solid State Ionics 178 (2007) 59–66.
[4] J. Lian, S.V. Yudintsev, S.V. Stefanovsky, L.M. Wang, R.C. Ewing, J. Alloys Compd. 444–445 (2007) 429–433.
[5] X.Q. Cao, R. Vassen, D. Stoever, J. Eur. Ceram. Soc. 24 (2004) 1–10.
[6] P.K. Moon, H.L. Tuller, Solid State Ionics 28–30 (1988) 470–474.
[7] J.W. Fergus, J. Power Sources 162 (2006) 30–40.
[8] S. Hui, J. Roller, S. Yick, X. Zhang, C. Decès-Petit, Y. Xie, R. Maric, D. Ghosh, J. Power Sources 172 (2007) 493–502.
[9] T. van Dijk, K.J. de Vries, A.J. Burggraaf, Phys. Status Solidi. A 58 (1980) 115–125.
[10] A.J. Burggraaf, T. van Dijk, M.J. Verkerk, Solid State Ionics 5 (1981) 519–522.
[11] K. Shinozaki, M. Miyauchi, K. Kuroda, O. Sakurai, N. Mizutani, M. Kato, J. Am. Ceram. Soc. 62 (1979) 538–539.
[12] K.V. Govindan Kutty, C.K. Mathews, T.N. Rao, U.V. Varadaraju, Solid State Ionics 80 (1995) 99–110.
[13] B.P. Mandal, S.K. Deshpande, A.K. Tyagi, J. Mater. Res. 23 (2008) 911–916.
[14] J.A. Díaz-Guillén, M.R. Díaz-Guillén, J.M. Almanza, A.F. Fuentes, J. Santamaría, C. León, J. Phys.: Condens. Matter 19 (2007) 356212.
[15] Z.-G. Liu, J.-H. Ouyang, Y. Zhou, J. Mater. Sci. 43 (2008) 3596–3603.
[16] Z.-G. Liu, J.-H. Ouyang, B.-H. Wang, Y. Zhou, J. Li, J. Alloys Compd. 466 (2008) 39–44.
[17] G.S. Rohrer, Structure and Bonding in Crystalline Materials, Cambridge University Press, Cambridge, 2004, pp. 521–525.
[18] D. Michel, M. Perez-y-Jorba, R. Collongues, Mater. Res. Bull. 9 (1974) 1457–1468.
[19] J.B. Goodenough, Annu. Rev. Mater. Res. 33 (2003) 91–128.
[20] J.R. Macdonald, W.B. Johnson, Fundamentals of impedance spectroscopy, in: E. Barsoukov, J.R. Macdonald (Eds.), Impedance Spectroscopy: Theory, Experiment and Applications, second edition, John Wiley & Sons, Inc., New Jersey, 2005, pp. 1–26.
[21] M.H. Abdullah, A.N. Yussof, J. Mater. Sci. 32 (1997) 5817–5823.